Chemie Ingenieur Technik

Chemie Ingenieur Technik

RESEARCH ARTICLE OPEN ACCESS

Integral Experiments and Magnetic Resonance Imaging of Lab-Scale Liquid Distributors

Hannah S. Rennebaum[1] | Alina Dobschall[2] | Jenni Bindseil[1] | Mirko Skiborowski[2] | Alexander Penn[1]

[1]Institute of Process Imaging, Hamburg University of Technology, Hamburg, Germany | [2]Institute of Process Systems Engineering, Hamburg University of Technology, Hamburg, Germany

Correspondence: Alexander Penn (alexander.penn@tuhh.de)

Received: 12 February 2026 | **Revised:** 10 June 2026 | **Accepted:** 2 July 2026

Keywords: integral experiments | lab-scale column | liquid distributor | magnetic resonance imaging

ABSTRACT

Liquid maldistribution in packed beds can significantly reduce process efficiency and is strongly influenced by the liquid distributor design. In this work, four lab-scale liquid distributors based on gravity- and pressure-driven operating principles were investigated at two liquid loads. Their performance was evaluated using flow maps and the maldistribution factor, revealing substantial differences between designs. The distributor providing the most homogeneous distribution was further analyzed regarding flow stability, gas load, and packing interaction. Compared to a single-point liquid distribution, the proposed distributor reduced maldistribution and wall flow. Magnetic resonance imaging measurements showed a progressive deterioration of the flow homogeneity along the packing height.

1 | Introduction

Packed bed columns are widely used in industries due to their ability to provide efficient gas–liquid contact under counter-current flow, making them particularly suitable for distillation, absorption, and other separation processes [1]. The hydrodynamics inside these beds, particularly the distribution of the phases, plays a critical role in determining the overall performance. Maldistribution remains a persistent challenge that can significantly reduce the efficiency of the process [2], with gas maldistribution generally being negligible compared to liquid maldistribution [3]. Liquid maldistribution has been quantified using a variety of experimental techniques, including wire mesh sensors [4, 5], tracer studies [5], and collector experiments [6, 7]. A comprehensive overview of experimental techniques for characterizing flow and mass transfer in packed beds has recently been provided by Hampel et al. [8].

Compared to other measurement techniques, which provide valuable information on liquid maldistribution but lack the ability to resolve the full three-dimensional, time-dependent flow structure within opaque packed beds, tomographic methods overcome this limitation. In the past, they have also been applied to detect and characterize maldistribution phenomena [8–10]. Another promising technique is magnetic resonance imaging (MRI). MRI has increasingly been employed as a noninvasive method for studying multiphase flow in packed beds. It has recently been used to measure maldistributions, particle wetting, and flow fields in trickle-bed columns [11]. In addition, MRI has been applied to investigate, among other aspects, voidage distribution [12], liquid holdup and surface wetting characteristics [13], as well as flow maps of liquid and gas phase in packed beds [14].

Maldistribution of liquid flow can arise from several factors, such as variations in the packing density for random packings,

Abbreviations: 3D, three-dimensional; AM, additively manufactured; FOV, field of view; MRI, magnetic resonance imaging; RF, radio frequency; SLA, stereolithography; STL, Standard Tessellation Language.

wall flows and channeling, discontinuities at seams between structured packing elements, and nonuniform initial fluid distribution at the column inlet [15, 16]. For structured packings, the liquid distributor is considered the most critical equipment and is expected to deliver the liquid uniformly over the cross section [17]. Improving the initial liquid distribution across the bed cross section, in particular, shortens the length required for the flow to achieve steady-state conditions [6].

To achieve a homogeneous initial liquid distribution, three distributor characteristics are particularly important: the density, position, and uniformity of the drip points—the outlets through which liquid enters the bed [18]. While distributor design determines the density and arrangement of drip points, their actual uniformity is often unknown and must be measured or estimated.

Various methods have been developed to assess the quality of the distributor design [19]. Because the initial liquid distribution strongly affects the downstream spreading behavior, quantitative tools are needed to evaluate whether a given distributor provides sufficient coverage and uniformity before it is implemented in a packed column. Moore and Rukovena [20] proposed a graphical method in which each drip point is associated with a surrounding circular area, determined by the ratio of the flow rate from that drip point to the total liquid flow rate. The resulting areas are then evaluated based on their coverage of the column cross section and the extent of overlap between neighboring drip points. Spiegel [21] introduced the wetting index as a measure for evaluating liquid distributors, allowing the evaluation of designs based on drip points or drip lines. For a given structured packing, the wetting index is determined by combining assumptions about the vertical spreading of liquid with the arrangement and number of drip points or drip lines. The wetting index and the graphical method provide practical design criteria, yet they rely on simplified spreading assumptions and offer limited insight into the spatial development of liquid maldistribution inside the packing.

Liquid distributors used in large-scale trickle bed reactors are commonly classified into four main types: (a) perforated tray, (b) chimney tray, (c) bubble cap tray, and (d) vapor-lift tube [22]. For packed bed columns, vendors provide selection guides for suitable spray and arm liquid distributors depending on liquid load and column diameter [23]. Regardless of the specific design, a sufficiently high drip-point density is essential for achieving a uniform initial distribution. For industrial-scale columns, a minimum drip point density of up to 160 m^{-2} is recommended [21, 24]. The minimum density depends on the specific surface area of the structured packing used, with higher areas requiring correspondingly higher densities [24]. The required drip point density decreases with increasing column diameter and with the use of higher-generation packings [19]. If the number of drip points falls below a system-dependent critical value, the number of theoretical stages per meter decreases [21], reducing the number of effective separation stages and lowering the overall column efficiency. Studies in large-diameter columns [25] further show that operating conditions, such as gas and liquid loads, typically have only a minor effect on liquid maldistribution compared to the influence of the distributor design itself.

The quality of the liquid distribution is considered to be of utmost importance for maldistribution [26]. Information on maldistribution in industrial columns cannot be directly extrapolated to pilot- or lab-scale systems. The smaller column diameters and heights in pilot- or lab-scale systems result in a significantly larger surface-to-volume ratio, which in turn alters the hydrodynamics. The modified geometry intensifies wall flow [23] and channeling, influences the residence times of the different phases, and can lead to increased heat losses [27]. Properly accounting for the potential efficiency-lowering effects of liquid maldistribution is a major concern for column designers in terms of scale-up considerations [17]. This also results in different requirements for a liquid distributor, with laboratory-scale columns generally requiring higher drip point densities than industrial-scale columns. Consequently, the design criteria and operational expectations for liquid distributors at laboratory scale differ substantially from those used in industrial practice.

At the laboratory scale, Ashour et al. [28] examined liquid distribution in a structured-packing column with a diameter of only 20 mm and found that, at low liquid loads, a single-point distributor can yield more uniform radial spreading than a three-point design, which tends to channel liquid toward the wall. At higher liquid loads, the distribution becomes less uniform, as the increased surface-to-volume ratio promotes stronger wall flow. These findings highlight the strong sensitivity of liquid spreading behavior to both distributor geometry and operating regime. Da Cunha et al. [29] designed a gravity-driven distributor with a tree-like configuration, where each outlet was equipped with a bundle of wires to disperse the water. Rather than increasing the number of outlet holes, they maintained the same number but extended each one using multiple wires to raise the number of irrigation points. This approach avoids adding outlets, which would otherwise increase both the risk of clogging and the pressure drop. The tree-like structure improved the separation efficiency for one type of structured packing, demonstrated by a reduced height equivalent to a theoretical plate compared to the orifice-pan distributor. These findings illustrate that even small modifications to distributor geometry can strongly influence the resulting flow distribution in columns of small scale.

Despite extensive studies on distributor effectiveness, systematic comparisons between integral measurement techniques—such as collector experiments—and spatially resolved imaging methods remain limited. In addition, few investigations have examined how the geometry of the distributor interacts with multiple operating conditions, packing types, and axial positions within the column. As a result, the mechanisms governing the evolution of liquid distribution downstream of the distributor are not yet fully understood.

This work addresses these gaps by combining collector experiments with MRI to evaluate and compare several liquid distributor configurations in a lab-scale column. The study covers four gas and two liquid loads, three distributor-to-collector distances, and two structured packings. MRI measurements provide detailed axial profiles of the liquid distribution, enabling a comparison with the data from integral experiments. To enhance reproducibility and support future research, all distributor designs are made publicly available as STL (Standard Tessellation Language) files suitable for stereolithography (SLA) 3D printing via

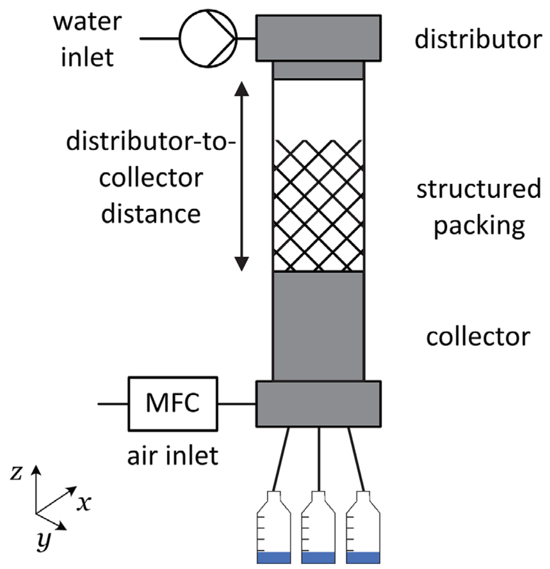

FIGURE 1 | Sketch of the experimental setup.

GitLab (https://collaborating.tuhh.de/projects/21352), enabling accurate replication and straightforward integration into other experimental setups.

2 | Methods

2.1 | Experimental Setup

The experimental setup (Figure 1) consists of a packed bed column built from a polymethyl methacrylate tube with an inner diameter of 54 mm and a wall thickness of 3 mm. The column height is adjustable via modular sections of varying lengths, which are connected by flanges. The top of the column remains open.

The column can be equipped with different internals, including a liquid distributor installed at the top and optional structured packings. Gas is introduced at the bottom of the column via a mass flow controller (Bronkhorst F-202AV-M20-AAD-44-V), while liquid is introduced at the top through the liquid distributor. For the integral experiments, a collector was mounted at the bottom of the column, functioning as both the gas inlet and the liquid outlet (Figure 1). For the MRI measurements, a bottom extension tube (length 300 mm, with an identical diameter to the column) was installed. A drainage tube serving as the liquid outlet was connected to its bottom, ensuring that the liquid column formed in the extension tube rather than in the structured packing within the field of view (FOV) of the MRI measurement. The specific internals used in the experiments are described in detail in the following sections.

2.1.1 | Liquid Distributors

Four liquid distributors with two operating principles, two pressure-driven and two gravity-driven designs, were evaluated (Figure 2). Three designs were constructed with 13 drip points (Figure 2a–c), resulting in a drip point density of 5676 $\frac{1}{m^2}$, which corresponds to the number of drip points per square meter. The drip points are uniformly distributed throughout the cross section of the column. The liquid collector and the distributor were aligned to ensure that each drip point corresponds to a segment of the liquid collector. The gas outlets were made as large as possible to minimize any impact on the liquid distribution. The liquid inlet, located at the center of the cross section, consists of a 1/2-in. thread connected to a tube with an outer diameter of 6 mm and an inner diameter of 4 mm. For the fourth design, which is adapted from the design of Da Cunha et al. [29], 60 drip points were arranged over the circular shape of the column (Figure 2d), resulting in a higher drip point density of 26,198 $\frac{1}{m^2}$. This also implies that, due to the tree-like structure, the drip points were not aligned with the different segments of the collector in comparison with the three other distributor designs.

Figure 2a,e and 2b,f shows the pressure-driven distributor in its two versions. Both distributors provide a total open area for the outflowing gas of 724 mm^2, corresponding to approximately 32% of the column cross section. The distributor design consists of channels that split from one into four in the first layer and further into 13 channels in the second layer. The 13 outlet channels, each with an inner diameter of 0.9 mm, are arranged in three concentric circles. One channel lies at the center of the column cross section, with four channel outlets arranged in a circular pattern at a distance of 11.5 mm from the center, and another eight channel outlets placed at a distance of 20.6 mm from the center. The two versions differ in the design of their outlet geometry. Version 1, referred to as Distributor 1 in the following, employs flat outlet channels, whereas version 2 (Distributor 2) features tapered outlets to reduce the contact area between the outlet and the liquid.

The first gravity-driven distributor (Figure 2c,g), referred to in the following as Distributor 3, has an open area of 938 mm^2, corresponding to 41% of the column cross section. The incoming liquid is first directed into four channels to promote a uniform initial distribution. It then collects inside the distributor until the liquid level reaches the height of the 13 outlets. The outlet geometry incorporates curved surfaces to reduce surface tension, while capillary structures at the outlet tips guide the liquid flow. Consistent with the pressure-driven design, the drip points—located at the ends of the capillaries—are arranged with one capillary at the center, four positioned at a radius of 11.5 mm, and eight positioned at a radius of 20.6 mm from the center.

The second gravity-driven distributor (Figure 2d,h) is adapted from a design proposed by Da Cunha et al. [29]. It features six liquid outlets, each 6 mm in diameter, arranged on a circular pattern with a diameter of 42 mm. At the center of each outlet, a single trunk extends outward and branches into a tree-like structure composed of three successive layers, each of height 5 mm. The first branching layer consists of three branches with a diameter of 1 mm; in each subsequent layer, every branch is divided into three new branches. The branching angle at each division point is 40°. To prevent individual drip points from

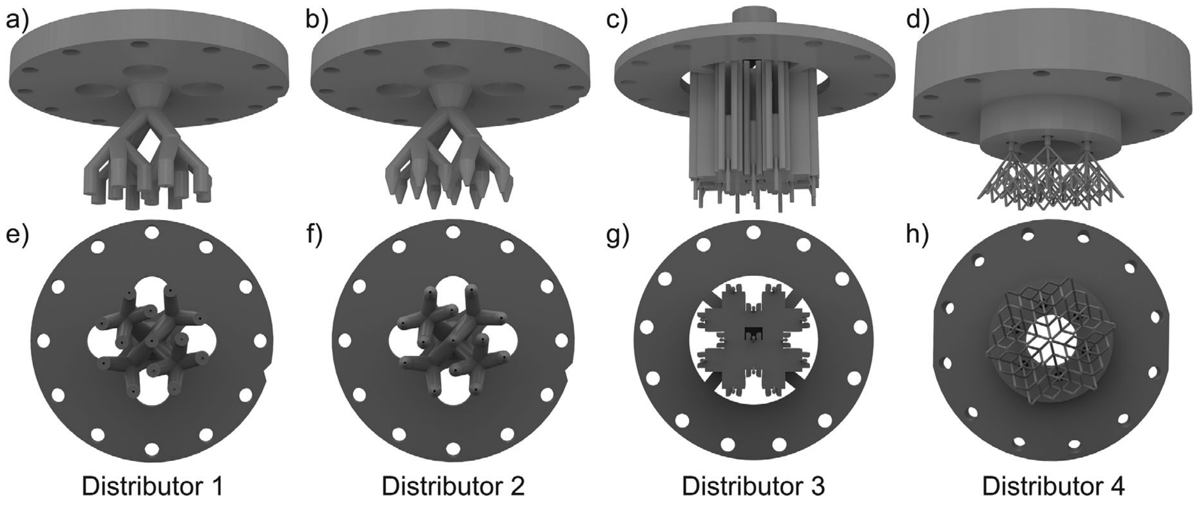

FIGURE 2 | The liquid distributors investigated in this study are shown in (a)–(d) in a side view and in (e)–(h) in a bottom view. The designs include in (a) and (b) a pressure-driven design with 13 outlet channels, available in two versions—one with flat liquid outlets (Distributor 1) and one with tapered liquid outlets (Distributor 2); and (c) and (d) two gravity-driven liquid distributor designs, comprising (c) Distributor 3 with a capillary-based structure and (d) Distributor 4 with a tree-like structure similar to the design proposed by Da Cunha et al. [29].

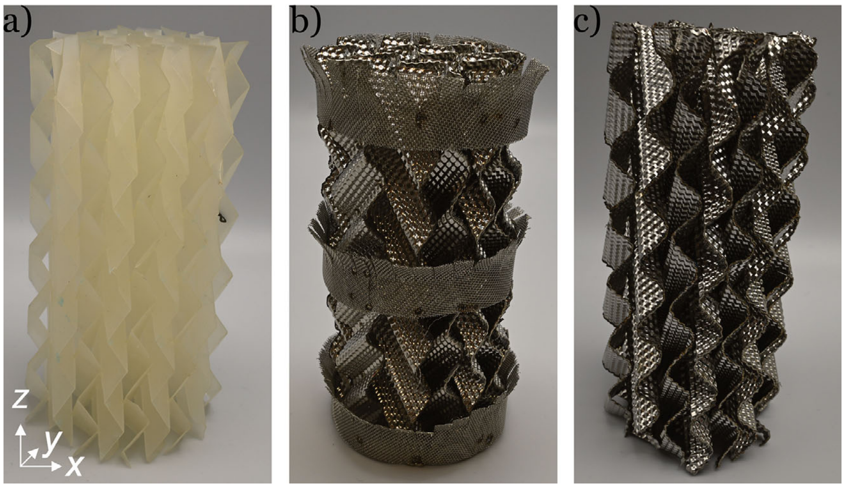

FIGURE 3 | Structured packings tested in combination with Distributor 2. All packings are corrugated sheet packings with a specific surface area of 480 $\frac{m^2}{m^3}$ with (a) an additively manufactured packing (AM), (b) a metal packing including wipers ($metal_{wipers}$), and (c) the same metal packing without wipers (metal). The metal packing is a commercially available structured packing of type Montz B1-500.

running dry, the branches are interconnected between layers. The gas outlet is positioned centrally, forming a circular opening with a total open area of 380 mm^2, corresponding to 17% of the column cross section.

All liquid distributors were additively manufactured on a Formlabs 3D printer, Form 3+, using Clear Resin V4. The system operates via SLA, and an adaptive slice thickness was selected to accommodate the geometry of the printed parts. After printing, all distributors were washed in an isopropanol bath to remove residual resin and subsequently UV-cured. To prevent individual channels in Distributors 1 and 2 from becoming blocked, residual resin was removed using a wire, followed by air and water flushing in both directions.

2.1.2 | Structured Packing

The liquid distribution was evaluated with two types of structured packings (Figure 3). A commercially available Montz B1-500 corrugated sheet packing (Figure 3b,c) and an additively manufactured version with the same design (Figure 3a). The specific surface area is 480 $\frac{m^2}{m^3}$. Both packing elements have a height of 100 mm. Further geometric parameters, such as the corrugation angle, of both packings are shown in detail in [30]. The additively manufactured packing differs from the commercial version in its sharper zigzag geometry, whereas the commercial design features rounded corners. In addition, the commercial packing includes wall wipers, while the additively manufactured version was produced without them. To improve comparability

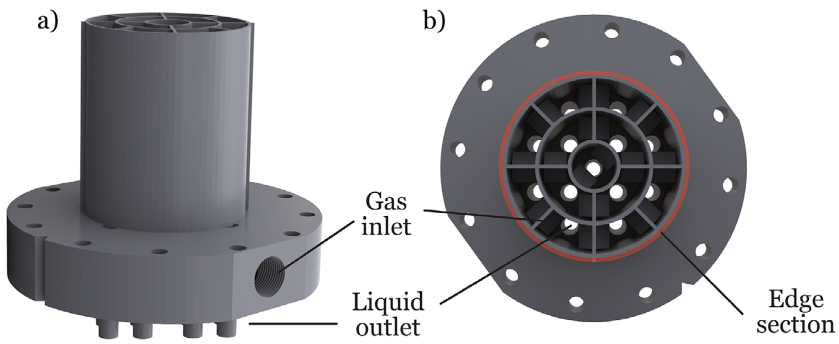

FIGURE 4 | Collector design used in the integral experiments to determine the liquid distribution at the column bottom: (a) side view and (b) top view. The edge section is highlighted by a semitransparent red ring.

between the packings, the Montz B1-500 was also tested without wall wipers (Figure 3c). Wall wipers, fabricated from flexible metal braiding for commercial packing, are used to reduce wall flow by redirecting liquid from the column wall back into the packing interior. The additively manufactured packing has a maximum diameter of 53 mm, while the commercially available packing without wipers has a maximum diameter of 47 mm. Neither design is perfectly circular because they are constructed from complete corrugated sheets, resulting in a stepped outer geometry. In contrast, the commercially available corrugated-sheet packing equipped with wipers fully adapts to the column diameter of 54 mm due to the flexibility of the wiper elements. The material thickness is 0.2 mm for the additively manufactured packing and 0.1 mm for the commercially available packing. For the commercially available metal packing, a water contact angle of $45.9 \pm 0.8\,^\circ$ was measured, while the additively manufactured packing exhibited a water contact angle of $70.4 \pm 1.2\,^\circ$. The additively manufactured packing was required for the MRI measurements, as MRI compatibility requirements restrict the use of metallic materials. Structured packings were included in the experimental setup used for the measurements presented in Figures 9 and 10.

2.1.3 | Liquid Collector

The liquid collector at the bottom of the column is designed to (a) gather liquid from the segments to measure the liquid distribution and (b) maintain a homogeneous countercurrent gas flow without disturbing the liquid collection. For this purpose, a special liquid collector (Figure 4) with 15 segments was constructed. Each segment has the same area of approximately 153 mm^2 and a height of 60 mm. Different segments are separated by walls of a thickness of 1 mm. The segments are arranged in three rings around the center segment. The first ring adjacent to the center segment consists of four segments, the second ring of eight segments, and the third and outer ring of two segments. The outer ring was constructed to capture the wall flow on the outside of the column. As the two segments in the outer ring remain unsealed, they are considered collectively as a segment of twice the area. Each segment includes a drainage as a liquid outlet with a diameter of 4.8 mm, which was large enough to allow the liquid to pass freely without the need for additional pumps to counteract the accumulating liquid column. Since the outer ring is less than 4.8 mm wide, the outlet was resized accordingly and duplicated to maintain a comparable outlet area. The gas was distributed through gas chimneys terminating 20 mm below the top of the collector, preventing the outflowing gas from obstructing the liquid entering a segment. The chimneys are integrated into the walls between adjacent segments of rings one and two, allowing all segments to share a tube with their neighboring segments. Due to the limited space, the outer ring does not have gas outlets. The center ring has two half tubes to fit the space. All gas outlets are covered by caps to prevent liquid from flowing out through the gas inlets. The collector was also additively manufactured with the same process as described in Section 2.1.1.

2.2 | Integral Experiments

The liquid distribution of the four distributor designs was evaluated in collector experiments with air and water as the material system. Each experiment was performed in triplicate, beginning once liquid emerged from the distributor and ending after 5 min or when one of the 1-L bottles beneath the collector segments was filled. For Distributors 1, 3, and 4, measurements were carried out without gas flow and at a fixed distributor-to-collector distance of 0 mm. The liquid load (Equation 1), B, defined as the liquid volume flow, $\dot{V}_L$, normalized by the column cross-sectional area, A_{column}, was tested at 5 and 20 $\frac{m^3}{m^2 h}$.

$$B = \dot{V}_L / A_{column.} \tag{1}$$

Distributor 2, identified as the design exhibiting the most uniform distribution, was examined over an extended parameter range with three distributor-to-collector distances of 0, 160, and 260 mm and four gas loads characterized by an F-factor (Equation 2) of 0, 0.4, 0.8, and 1.2 $\sqrt{Pa}$. The gas volume flow was varied between 50, 100, and 150 $\frac{L}{min}$ under standard conditions (1.01325 bar and 298.15 K), corresponding to superficial gas velocities (υ_{gas}) of 0.36, 0.73, and 1.09 $\frac{m}{s}$ or a volumetric flow rate at normal conditions (1.01325 bar and 273.25 K) of 2.75, 5.5, and 8.25 $\frac{Nm^3}{h}$, respectively, calculated using the ideal gas law. A gas density, ρ_{gas}, of 1.204 $\frac{kg}{m^3}$ at standard conditions was assumed.

$$F = \upsilon_{gas} \sqrt{\rho_{gas}}. \tag{2}$$

TABLE 1 | Experimental parameters for the spin density MRI measurements.

Scan parameter	Spin density
Orientation	Horizontal
Field of view	64 mm × 64 mm × 105 mm ($x \times y \times z$)
Scan duration	34 s
Spatial resolution	1 mm × 1 mm × 1 mm
Flip angle	20°
Repetition time	4.6 ms
Echo time	3.8 ms

The tested F-factors are well below the potential flooding point, which was determined optically for the experimental setup, including the additively manufactured packing. For liquid loads of 5 and 20 $\frac{m^3}{m^2 h}$, flooding was observed at gas volume flows of 425 and 500 $\frac{L}{min}$, respectively. The two structured packings were investigated at a distributor-to-collector distance of 260 mm and liquid loads of 5 and 20 $\frac{m^3}{m^2 h}$ without gas flow. Their distribution quality was compared to a reference distribution generated by a central tube outlet with an inner diameter of 4 mm, providing a drip point density of 436 $\frac{1}{m^2}$.

2.3 | Magnetic Resonance Imaging

MRI is a tomographic technique that can be used to quantify liquid distribution in opaque columns. Because the MRI signal originates from hydrogen nuclei in the liquid phase, the measured signal intensity is proportional to the local liquid holdup [31]. In this study, MRI was employed to determine the liquid distribution along the height of the structured packing. The liquid within the packing can be divided into static and flowing. Because static liquid does not influence the liquid flow through the packing, its contribution to the MRI signal is minimized. The signal from static liquid is suppressed by keeping the longitudinal relaxation time T_1 of the aqueous solution to around 600 ms (Spinsolve 60 MHz, Magritek) and thereby relatively high (deionized water with a copper sulfate concentration of 2 mM) and reducing the repetition time T_R to a value of 4.6 ms. When the repetition time—i.e., the interval between consecutive spin excitations—is much shorter than the relaxation time, which is required for a substantial fraction of the spins to return to equilibrium for efficient re-excitation, the measured signal intensity becomes low in regions containing predominantly static liquid. In contrast, in regions with flowing liquid, new spins continuously enter the measurement area and can still be effectively excited. The echo time T_E is kept short to ensure that the flowing liquid does not leave the selected slice before the signal is recorded. To enhance the captured signal-to-noise ratio, a tailored radio frequency (RF) detection array was used, built as an 8-leg low-pass birdcage design with an inner diameter of 80 mm. Important MRI parameters are summarized in Table 1.

The MRI measurements were acquired at a 3-T vertical MRI system (Tesla Engineering Ltd., UK), which included a high-performance gradient coil (Tesla Engineering Ltd., UK), a birdcage RF coil (Tesla Dynamic Coils, The Netherlands), and a medical backend (Philips Medical Systems, The Netherlands). The measurements were performed using a fast field echo sequence with frequency encoding applied along the x-direction. The FOV was positioned such that the structured packing was centered within it. As the FOV measured 105 mm while the packing extended over 100 mm, slices outside the packing region were subsequently excluded from the analysis. Each measurement includes a single scan per slice within the structured packing. The distance between the distributor and the structured packing was 160 mm. The measurements were carried out under steady-state conditions. Between repeated measurements, the pump was turned off to allow the flow to redistribute and reach a new steady-state pattern. All measurements were conducted in prewetted structured packings.

2.4 | Data Evaluation

The maldistribution factor, M_f, was used to evaluate the liquid distribution obtained from integral experiments and MRI measurements (Equation 3) [19]. It is defined as the sum of the deviations of liquid load in each segment, $u_{L,i}$, from the average liquid load, u_L, and weighted by the ratio of the segment area, A_i, to the area of all segments, A.

$$M_f = \sum_{i=1}^{n} \left| \frac{u_{L,i} - u_L}{u_L} \right| \frac{A_i}{A}. \tag{3}$$

Depending on the liquid distribution, the maldistribution factor can vary between 0 and 2, where 0 represents a perfectly homogeneous distribution and 2 represents the most nonuniform (highly maldistributed) case. Measurements conducted without packing are analyzed excluding the edge segments, whereas measurements with structured packings include the edge segments. The maldistribution factor calculated from the 13 central segments (excluding the edge segments) is hereafter referred to as $M_{f,13}$, while the maldistribution factor calculated from all 15 segments is referred to as $M_{f,15}$.

For the MRI measurements, the wall flow and maldistribution factor were calculated independently for each slice with a slice thickness of 1 mm and then averaged over eight slices along the column height. The data were masked using a threshold-based method and overlaid with the same segments used for the collector. Pixel clusters containing fewer than 10 pixels were excluded from the liquid classification and reassigned to the gas phase to prevent noise from being misclassified as liquid. For each segment, the mean pixel intensity was calculated and used as a measure of the local liquid holdup. These values were then used to determine the wall flow and maldistribution factor.

3 | Results and Discussion

3.1 | Liquid Distributor

The flow distribution quality of the different distributor designs (Figure 2) is evaluated using the maldistribution factor, which is obtained from integral experiments conducted at two different

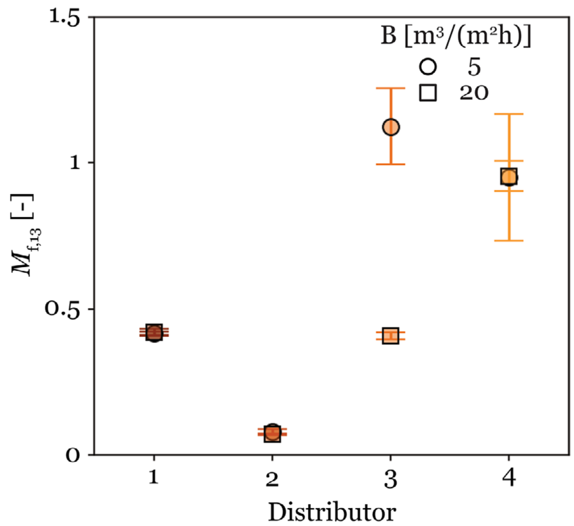

FIGURE 5 | Maldistribution factor for various liquid distributor designs measured at two liquid loads, 5 and 20 $\frac{m^3}{m^2 h}$. The marker shapes indicate the liquid load, while marker colors distinguish the distributor designs. Distributors 1 and 2 are pressure-driven distributors featuring flat channels (Figure 2a,e) and tapered channels (Figure 2b,f), respectively. Distributors 3 and 4 are gravity-driven distributors, employing a capillary structure (Figure 2c,g) and a tree-like structure (Figure 2d,h) similar to the configuration described by Da Cunha et al. [29]. Measurements were conducted with a distributor-to-collector distance of 0 mm, without any structured packings included.

liquid loads directly beneath the drip points. The edge segments of the liquid collector are excluded from the maldistribution analysis, as the distributor designs intentionally include no drip points in these regions in order to prevent wall flow. Figure 5 presents the maldistribution factor displayed above the corresponding liquid distributor design. The measurements demonstrate that the liquid distributor design has a strong influence on the homogeneity of the liquid distribution. The pressure-driven designs (Distributors 1 and 2) exhibit low maldistribution factors compared to the gravity-driven designs (Distributors 3 and 4), indicating effective liquid distribution.

Distributors 1 and 2 show no dependence on liquid load. Furthermore, the low standard deviations obtained from triplicate measurements confirm the high reproducibility of the resulting liquid distribution. Although both channel designs provide a homogeneous initial liquid distribution, the design of the liquid outlet tip has a strong influence on the overall efficiency. The flat outlet of Distributor 1 leads to a less homogeneous flow distribution than the tapered design of Distributor 2. This behavior can be attributed to the larger contact area between the exiting liquid and the distributor structure in Distributor 1. A larger contact area enhances the relative influence of surface tension, resulting in less uniform performance of the drip points. Some drip points produce droplets with reduced flow, while others exhibit strong jet formation with increased flow. In contrast, Distributor 2 predominantly produces stable liquid jets rather than droplets. This difference is also evident from a comparison of Figure 6a,b, which shows example photographs of the water flow for the two distributor designs. Both pressure-driven designs risk clogging as a result of their small outlet diameters, thereby reducing the homogeneity of the liquid distribution.

The gravity-driven distributors lead to a less homogeneous distribution than the pressure-driven designs, as evidenced by $M_{f,13}$ exceeding one. Distributor 3 is strongly influenced by the liquid load: at low liquid loads, an $M_{f,13}$ of 1.2 is observed, while at high liquid loads the $M_{f,13}$ decreases to 0.4, which lies within the range observed for Distributor 1. This behavior is explained by Figure 6c, where only three capillaries form a continuous liquid jet, whereas the remaining capillaries show droplet formation or remain completely non-wetted at the low liquid load. The edges at the side outlet of each drip point generate strong surface tension. Once the liquid overcomes this surface tension at a single point, a preferential flow path is established, and the subsequent liquid follows the same path. At high liquid loads, the liquid flow is sufficient to overcome the surface tension at multiple side outlets simultaneously.

Distributor 4 again exhibits a similar liquid distribution that is largely independent of liquid load, with an $M_{f,13}$ of approximately 0.95. The poor liquid distribution is evident in Figure 6d, where the tree-like structure is only partially wetted. The already wetted regions subsequently serve as preferential pathways for the incoming liquid flow. Compared with the maldistribution factors reported by Da Cunha et al. [29], which range from 0.13 to 0.287, the values obtained in the present study appear to be considerably higher. However, this difference can be attributed to several factors. First, the maldistribution factor was defined differently, resulting in a value range between 0 and 1. When the same distributions are evaluated using Equation (3), values between 0.37 and 1.65 are obtained, which encompass the range measured here for Distributor 4. Second, the experimental conditions differ: Da Cunha et al. measured the liquid distribution after 1 m of packed bed using a Tetra Spline packing, not the initial liquid distribution by the distributor. In addition, their experiments were conducted at a slightly higher liquid load and with a larger column diameter (150 mm vs. 54 mm here).

The enhanced uniformity of drip points observed in pressure-driven distributor designs can be attributed to the higher driving forces at the outlets compared to gravity-driven distributors. In gravity-driven designs, the reduced driving force increases the sensitivity of the flow to geometric imperfections, surface tension effects, and local wetting conditions. In contrast, pressure-driven distributors exhibit more stable and continuous liquid jets, as capillary resistance is overcome by a higher and more uniformly distributed pressure drop across all drip points.

In addition to $M_{f,13}$ as a metric for comparing different liquid distributors, flow distribution maps (Figure 6e–l) provide further insights into the spatial locations of liquid maldistribution. For Distributors 1 and 2, the flow distribution maps obtained at high and low liquid loads are very similar, consistent with the comparable maldistribution factors. Distributor 2 exhibits a maximum flow deviation of less than ±20%. No systematic tendencies, such as individual quarters or concentric rings with increased or decreased liquid flow, are observed. In contrast, Distributor 1 exhibits an unequal liquid distribution between different quarters at both investigated liquid loads. The collected liquid content is reduced in the lower-left quarter, while it

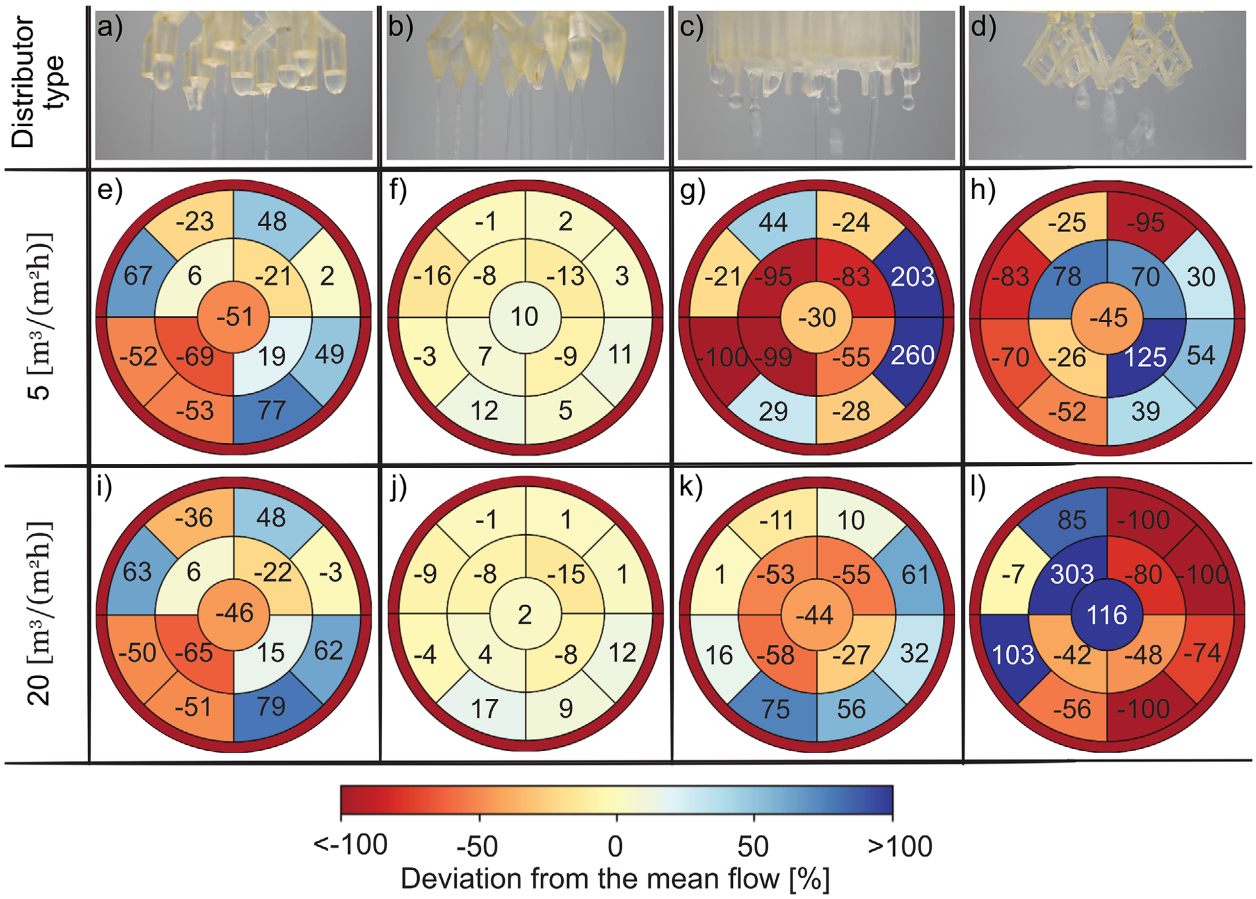

FIGURE 6 | Measurements and photographs of the four investigated liquid distributors arranged by column. Columns 1–4 correspond to Distributor 1, Distributor 2, Distributor 3, and Distributor 4, respectively. Panels (a)–(d) show photographs of the flow behavior at a liquid load of 5 $\frac{m^3}{m^2h}$. Panels (e)–(l) present flow distribution maps illustrating, for each segment, the average deviation from the mean flow at two liquid loads: (e)–(h) the low load (5 $\frac{m^3}{m^2h}$) and (i)–(l) the high load (20 $\frac{m^3}{m^2h}$). Measurements were conducted with a distributor-to-collector distance of 0 mm, without any structured packings included.

is increased in the lower-right quarter relative to the average liquid content. For Distributor 3 (Figure 6g,k), the liquid flow is concentrated in the outer concentric ring, while the five central segments exhibit reduced liquid load in comparison. This indicates that the central side outlets hinder the liquid from flowing out compared to the outer outlets. Additionally, for both liquid loads, higher local flow rates are observed in the lower half of the collector. For the high liquid load, the mean deviations in this half are 75%, 56%, 32%, and 61% for the outer ring and −27% for the inner ring. These observations indicate a higher local liquid content in the lower half and underline the strong influence of the experimental setup's alignment: even minor deviations from a vertical alignment result in an uneven liquid distribution, with increased liquid accumulation in one half of the column. Compared to Distributors 1 and 2, for which the average standard deviation between triplicate measurements across all drip points is 2.8% and 1.2%, respectively, Distributor 3 shows a substantially higher average standard deviation of 37.2%. In contrast, the channel-based structures produce highly consistent flow distributions, and variations in flow between individual drip points can largely be attributed to minor printing inaccuracies, such as small differences in the internal diameters of the channels. By comparison, the liquid distribution of Distributor 3 is strongly influenced by the initial wetting of the structure, with subsequent liquid preferentially following the flow paths established by the first liquid. The influence of established flow paths is even more pronounced for Distributor 4, which is based on the design described by Da Cunha et al. [29]. This distributor exhibits the highest average standard deviation, at approximately 50%.

3.2 | Distributor-to-Collector Distance

For further evaluation of Distributor 2, which exhibited the best and most uniform distribution, integral experiments were conducted at three different distributor-to-collector distances, enabling assessment of how effectively the drip points concentrate the liquid to maintain a defined jet shape. If the liquid is more dispersed into droplets, it can be easily deflected and may enter one of the neighboring segments. As indicated by the maldistribution factor, the homogeneity of the liquid distribution decreases with increasing distributor-to-collector distance (Figure 7). In addition, the reproducibility of the liquid distribution—quantified by the standard deviation of repeated measurements—decreases with increasing distance and decreasing liquid load. For a distributor-to-collector distance of 160 mm, $M_{f,13}$ increases from 0.07 to 0.27 and 0.13 for the low and high

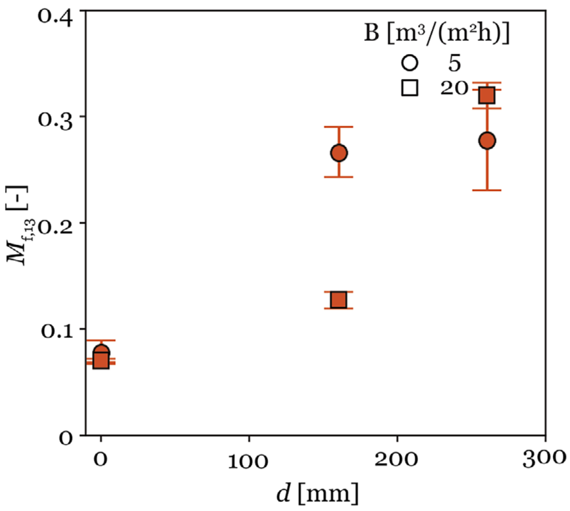

FIGURE 7 | Maldistribution factor as a function of the distributor-to-collector distance, d, measured using Distributor 2 at two liquid loads, 5 and 20 $\frac{m^3}{m^2h}$. The marker shapes distinguish the liquid load. Measurements were conducted without any structured packings included.

liquid loads, respectively. At this distance, the liquid load influences the distribution. A high liquid load increases the pressure in the liquid distributor, resulting in a liquid jet with increased velocity. For both liquid loads, Plateau–Rayleigh instabilities generate surface perturbations that ultimately lead to droplet formation [32]. These perturbations and the subsequent breakup into droplets reduce the jet focus and promote lateral spreading across multiple segments, thereby impairing the homogeneity of the liquid distribution. At higher liquid loads, the increased jet velocity shifts the onset of these instabilities further downstream from the drip point, resulting in improved homogeneity for a distributor-to-collector distance of 160 mm. Nevertheless, even at the largest distributor-to-collector distance, the maldistribution remains lower than the best value obtained for any of the other liquid distributors tested (Figure 5). Consequently, a short distance between the distributor and the packed bed beneath it is not only advisable to not waste valuable height of the column but also to obtain the most homogeneous liquid distribution.

3.3 | Gas Load

In addition to the liquid-only tests, further experiments were carried out under different gas loads to investigate how countercurrent flow influences liquid distribution and to better approximate real process conditions. Three gas loads (0.4, 0.8, and 1.2 $\sqrt{Pa}$) were investigated and compared with the no-gas reference case. As shown in Figure 8a, the maldistribution factor indicates that low gas loads enhance the homogeneity of the liquid distribution. At a gas load of 0.4 $\sqrt{Pa}$, the $M_{f,13}$ decreases to approximately 0.2. This trend is observed for both high and low liquid loads. When the gas load is further increased, the high liquid load of 20 $\frac{m^3}{m^2h}$ maintains a stable and homogeneous distribution of the liquid. In contrast, at the low liquid load of 5 $\frac{m^3}{m^2h}$, the liquid distribution becomes less homogeneous at the highest gas load of 1.2 $\sqrt{Pa}$, with a $M_{f,13}$ of 0.28, resembling the distribution observed without gas flow. These findings suggest

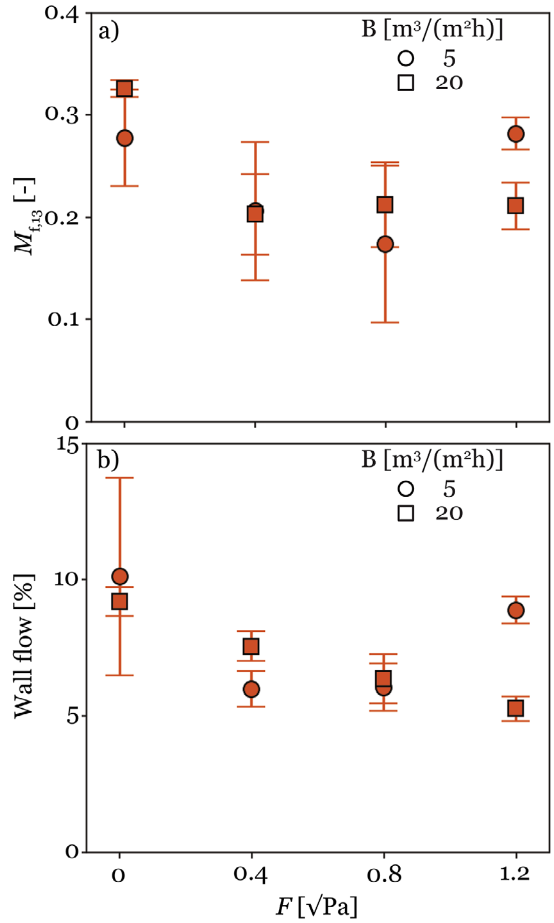

FIGURE 8 | Impact of the gas load, F, on (a) the maldistribution factor and (b) the wall flow for Distributor 2 at two liquid loads, 5 and 20 $\frac{m^3}{m^2h}$. The distributor-to-collector distance is 260 mm. Marker shapes indicate the respective liquid loads. Measurements were conducted without any structured packings included.

that low gas loads stabilize the liquid jet and help prevent unraveling. At higher gas loads, this stabilizing effect persists only when the liquid load is sufficiently high. For the low liquid load, where the liquid jet is inherently less stable—as confirmed by the distance measurements (Figure 7)—the jet becomes frayed under high gas loads.

Because the maldistribution factor does not include the two edge segments, the wall-flow quantity within these segments is evaluated separately (Figure 8b). Given that all segments have the same area, the expected share of flow through the two edge segments out of the total 15 is about 13%, corresponding to $\frac{2}{15}$. Because liquid accumulates almost exclusively in the edge segments due to wall flow, the objective is to minimize the flow in these segments rather than to reach the 13% associated with a uniform distribution. The amount of wall flow is largely independent of the liquid load for gas loads between 0 and 0.8 $\sqrt{Pa}$. At the high liquid load, the wall-flow quantity decreases with increasing gas load. The low liquid load exhibits a trend similar to that observed for the maldistribution factor in the inner segments of the liquid collector: small gas loads of 0.4 and 0.8 $\sqrt{Pa}$ reduce the wall-flow quantity, whereas the highest gas load of 1.2 $\sqrt{Pa}$ returns it to a level comparable to that of the case without gas flow. One possible explanation for the observed wall-flow behavior is that the liquid is introduced in the center of the column. This results in a higher liquid holdup and, consequently, an increased flow resistance in the central region. The gas phase is therefore preferentially directed toward the wall region of the column. The gas flow hinders the liquid from flowing into the wall region. As the gas load increases further, the previously described Plateau–Rayleigh instabilities are accompanied by Kelvin–Helmholtz instabilities arising from velocity differences at the fluid interfaces [33]. Together, these effects promote droplet formation, increasing the likelihood that liquid penetrates the wall region of the column.

3.4 | Structured Packing

Ultimately, the distributor provides the initial distribution for a structured packing. It is therefore important to know how well the initial distribution is maintained, knowing that some degradation is expected, varying with the type and size of the packing as well as the operating conditions [34]. Therefore, two different kinds of corrugated sheet packings are tested to investigate the initial distribution, in the first packing element, almost below the distributor, also comparing the results of Distributor 2 with those of a single drip point outlet from a central tube. Relative to the reference measurement with an empty tube, the initial distribution of Distributor 2 deteriorates when either packing is installed, as both packings increase the maldistribution factor (Figure 9a) and therefore yield a less homogeneous liquid distribution. Among the two, the 3D-printed replica (AM) of the corrugated-sheet packing results in the poorest liquid uniformity. The metal packing shows slightly better performance, with the version without wipers (metal) providing the most favorable distribution. This is primarily attributed to the final row of wipers, which ends directly above the collector. As a result, the flow is redirected from the wall region to the second ring from the outside, leading to an increased average liquid flow in this ring and, consequently, an increase in the maldistribution factor. Apart from the effect of the wipers, the observed differences between AM and metal packings are attributable to variations in surface properties and microstructure, while the sheet macrostructure remains identical. The metal packing is more hydrophilic, promoting improved spreading of the liquid. This is consistent with the lower contact angle of the metal packing, indicating improved wettability and increased adhesion of the aqueous phase to the surface. Additionally, the metal surfaces exhibit a characteristic roughness that further enhances wettability and contributes to the improved distribution. If the liquid is initially supplied via a centrally positioned tube, the liquid distribution measured at the bottom of the column is less uniform than that obtained with Distributor 2. This demonstrates that a basic central distribution approach in lab-scale columns is insufficient for making effective use of the cross-sectional area, at least for the initial elements of the packed bed.

Although the plastic packing showed only a marginally worse maldistribution factor in the central segments than the metal packing, the behavior with respect to wall flow differs significantly. The metal packing with wipers exhibits a wall-flow quantity similar to that of the empty tube, while the packing without wipers shows a slightly higher wall flow. In contrast, the 3D-printed packing exhibits a wall-flow quantity exceeding 50%. Distributor 2 results in a significantly better initial distribution than the central tube. This also results in a lower maldistribution factor for the different packings, as well as a lower wall flow for the metal packing. However, the distributor does not have a considerable effect on the increased wall flow for the AM packing. Overall, it becomes apparent that both the maldistribution factor and the wall flow should be considered to evaluate the homogeneity of the distribution.

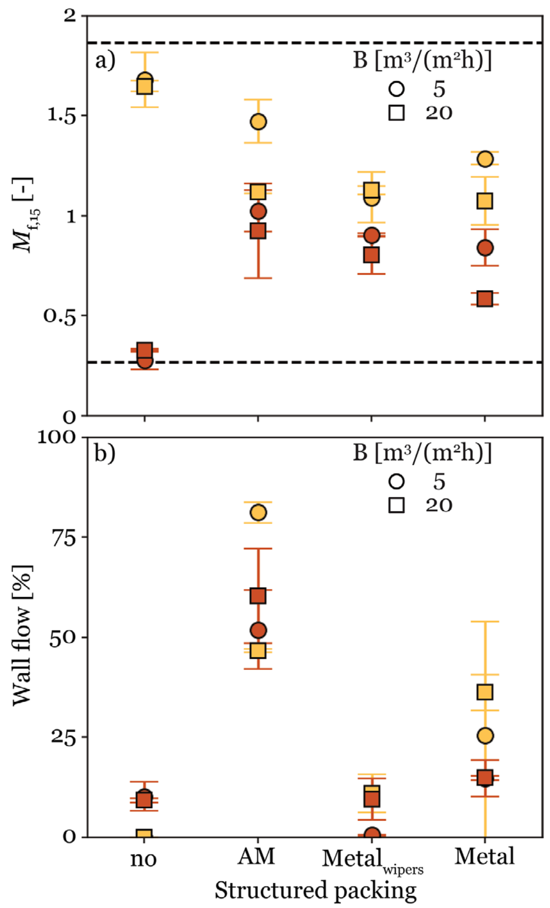

FIGURE 9 | Impact of the investigated structured packings on (a) the maldistribution factor and (b) the wall flow for Distributor 2 (red) and a central tube outlet (yellow) at two liquid loads, 5 and 20 $\frac{m^3}{m^2 h}$. The distributor-to-collector distance is 260 mm, and all packings have a height of 100 mm. Marker shapes indicate the respective liquid loads. The label "no" refers to measurements performed without any packing. The AM packing is a 3D-printed corrugated sheet packing. The $metal_{wipers}$ and metal packings correspond to the same metallic corrugated sheet packing, used with ($metal_{wipers}$) and without wipers (metal). The upper horizontal line represents the most inhomogeneous liquid distribution measured with the collector used in this study, where the entire liquid flow exits through a single segment. The lower horizontal line indicates the most homogeneous liquid distribution, occurring when no wall flows is present, and the edge segments remain empty.

3.5 | Magnetic Resonance Imaging

The MRI measurements (Figure 10a) provide insight into the development of the liquid distribution along the height of the

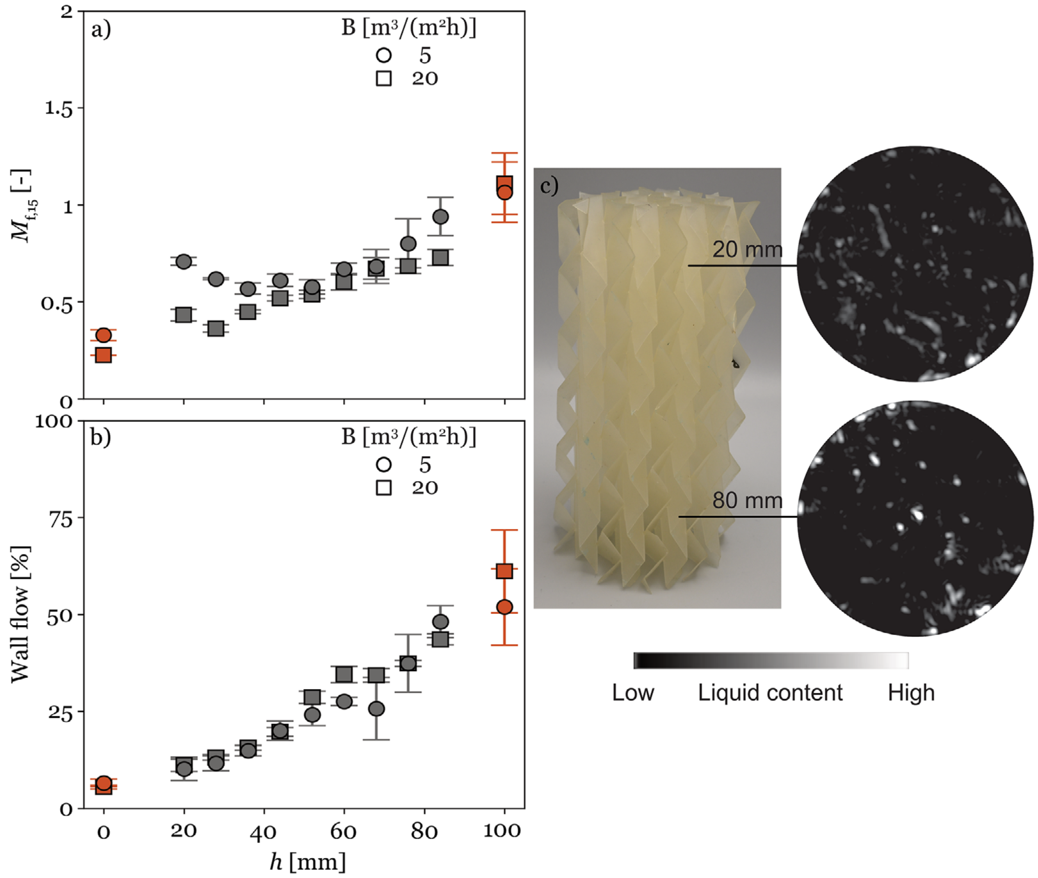

FIGURE 10 | Impact of the vertical position (height), h, within a 3D-printed corrugated sheet packing on (a) the maldistribution factor and (b) the wall flow for Distributor 2 without gas load at two liquid loads, 5 and 20 $\frac{m^3}{m^2 h}$. The distributor-to-collector distance is 260 mm. Marker shapes indicate the respective liquid loads. Red markers represent values obtained from integral experiments, while gray markers correspond to measurements acquired via MRI. The standard deviation was calculated from the triplicate measurements. (c) Corrugated sheet packing and exemplary slices of the MRI measurements at heights of 20 and 80 mm for a liquid load of 20 $\frac{m^3}{m^2 h}$.

structured packing. To validate the use of spin density measurements for determining the maldistribution factor and the wall flow, the MRI data are compared with results from integral experiments (Figure 10b,c). These reference measurements include the inlet distribution of the liquid at a distance of 160 mm and the end distribution at the outlet of the AM packing. The maldistribution factor obtained from the integral experiments increases from approximately 0.22 (high liquid load) and 0.33 (low liquid load) upstream of the packing to 1.11 and 1.06 downstream of the packing. Two limiting effects hinder the evaluation of the MRI measurements over the full packing height: low signal intensity at the packing inlet and high signal intensity at the packing edges between successive structured packing elements. Although the liquid flow rate remains constant along the packing height, these deviations in signal intensity arise for two reasons. The reduced signal at the top results from freely falling inlet liquid, which traverses the measurement region too quickly to be detected, thereby lowering the overall signal intensity. In contrast, the increased signal intensity between successive structured packing elements is caused by liquid accumulation in these regions. Although the MRI sequence suppresses static water, excessive accumulation is still detected, which artificially improves the apparent homogeneity of the liquid distribution. Consequently, the MRI measurements can only be reliably evaluated in the region where the signal intensity is approximately constant, corresponding to the structured packing between 16 and 88 mm from the top.

The data from the integral experiments and the MRI measurements exhibit similar trends. Because the data are not recorded at the same position, they are not directly comparable. For the low liquid load, the maldistribution factor calculated from the MRI data ranges from 0.57 to 0.94, whereas for the high liquid load it ranges from 0.36 to 0.73. The decrease in the maldistribution factor observed at low liquid load at the top of the packing could be related to the reduced MRI signal intensity in the upper column region described above. Due to the low liquid content, this artifact has a stronger impact on the calculated maldistribution, as individual flow channels contribute more significantly to the result. The apparent improvement in the distribution at the inlet of the structured packing is therefore not interpreted as a physical effect. For both liquid loads, $M_{f,15}$ increases more slowly at the top of the packing than toward the bottom. The MRI measurements indicate a slightly more homogeneous liquid distribution at the high liquid load compared to the low liquid load. A higher degree of homogeneity for high liquid loads is observed in the integral experiments directly below the liquid distributor as well. Below the packing, the integral experiments show no clear difference between high and low liquid loads, although the error bars at this location indicate a relatively large uncertainty in the value of $M_{\mathrm{f},15}$.

The wall flow determined from the integral experiments increases from 6% and 5% to 52% and 60% for the low and high liquid loads. The MRI measurements fit in well here with a minimum value of 10% and 11% and a maximum value of 48% and 44% for the low and high liquid loads, respectively. Similar to the maldistribution factor, the wall flow increases slowly at first and then more sharply. The MRI measurements reveal no clear trend with respect to the liquid load. The MRI measurements show that the wall flow increases continuously for the AM replica, resulting in a severe wall flow, which is considerably larger than that of the conventionally manufactured corrugated sheet metal packing. As previously described, both packings share the same macrostructure, while having different surface properties and microstructures. Both are obviously of significant importance to avoid large local acceleration of the liquid, which was apparently a reason for liquid spilling from the packing to the wall.

4 | Conclusion

Integral experiments and MRI measurements were conducted to examine the liquid distribution achieved by different liquid distributor designs. Four distributors were investigated: two based on gravity-driven operation and two based on pressure-driven operation. Measurements were performed at two liquid loads of 5 and 20 $\frac{\mathrm{m}^3}{\mathrm{m}^2\mathrm{h}}$. The results showed that the distributor design strongly influences the homogeneity of the liquid distribution, while the effect of liquid load was minor for most of the designs. The channel-structured, pressure-driven design, which provided the most homogeneous liquid distribution with a maldistribution factor of just 0.07, was used to investigate additional parameters, such as the varying gas loads, the distributor-to-collector distances, and the initial distribution in two different structured packings. The quality of the liquid distribution improved with increasing gas load up to 0.8 $\sqrt{\mathrm{Pa}}$. At the highest tested gas load of 1.2 $\sqrt{\mathrm{Pa}}$, the distribution quality deteriorated again at low liquid loads, while it remained essentially constant at high liquid loads. With increasing distributor-to-collector distance, the homogeneity decreased but remained within a solid range. Both corrugated sheet packings showed an increase in maldistribution from the excellent initial liquid distribution, which also aligns with the expectations [34]. However, the 3D-printed packing additionally led to a significantly pronounced increase in wall flow. The increase in liquid maldistribution along the height of the structured packing was additionally measured using MRI. The results were in good agreement with the integral experiments and indicated a slight decrease in homogeneity at the top of the packing, followed by an increasingly pronounced decrease toward the bottom.

In future work, the distributors could be tested with an alternative material system of differing polarity, such as long-chain alcohols, to assess whether the lower polarity—and thus lower surface tension—enhances the efficiency of gravity-driven designs. In addition, it should be examined whether differences in surface properties between metal and 3D-printed packings account for the observed differences in maldistribution. If this is the case, surface treatments may offer a means to improve the performance of the plastic packing. To further improve the MRI measurements, the magnetic susceptibility of the liquid, gas, and packing material can be matched. Differences in magnetic susceptibility between phases lead to local distortions of the magnetic field at their interfaces, which in turn cause signal loss and image artifacts. By minimizing these susceptibility differences, such field inhomogeneities are reduced, enabling a more accurate and undistorted representation of the interfaces between the materials. In addition to using MRI measurements to determine liquid distribution, such as by calculating the maldistribution factor and wall flow, the data can also be used to extract parameters like the interfacial area, which has a significant impact on process efficiency. Furthermore, MRI measurements can be extended to include liquid velocity data, enabling a clear distinction between stagnant and flowing zones. In the present study, all measurements were performed in prewetted structured packings. Future work could systematically examine wetting history effects by varying the initial saturation state, for example, including dry initialization, which may affect local phase distributions due to hysteresis associated with pore-scale filling processes. Singh et al. [35] previously simulated the impact of wetting history on interfacial area as a function of the tested liquid and liquid load. They showed that at low liquid loads, for a 0.1 M sodium hydroxide solution, which exhibits surface tension and viscosity values similar to water, prewetting increases the interfacial area. An increase in interfacial area may, in turn, be expected to influence the liquid distribution, which motivates further investigation.

Acknowledgments

The authors gratefully acknowledge Fin Conje for his contributions to the design of the tree-like structure, Till Lenczyk for performing the T_1-measurement for the used aqueous solution, and Stefan Benders for his support with the MRI measurements. Additionally, we would like to thank the Institute of Solids Process Engineering and Particle Technology at Hamburg University of Technology, and especially Maike Orth, for providing the measurement equipment and for their support in determining the contact angle of the structured packing material.

Open access funding enabled and organized by Projekt DEAL.

Funding

This project is funded by the Deutsche Forschungsgemeinschaft (DFG, German Research Council), grant number: 544956881 and SFB 1615 - 503850735, and by Hamburg University of Technology, I^3-Junior-Project entitled “Investigation of distributor designs for an enhanced liquid distribution in structured packings for thermal separation processes.”

Declaration of Generative AI and AI-Assisted Technologies in the Writing Process

This manuscript was copy-edited with the assistance of AI technology (ChatGPT, version 5.2) to enhance clarity and readability. All suggested edits were carefully reviewed by the authors, who take full responsibility for the final content.

Conflicts of Interest

The authors declare no conflicts of interest.

Data Availability Statement

Data will be made available on request.

References

1. D. Flagiello, A. Parisi, A. Lancia, and F. Di Natale, "A Review on Gas-Liquid Mass Transfer Coefficients in Packed-Bed Columns," *ChemEngineering* 5, no. 3 (2021): 43.

2. S. Lothar, "The Maldistribution Story - An Industrial Perspective," *Chemical Engineering Transactions* 69 (2018): 715–720.

3. R. Stikkelman, H. Teeuw, H. Wesselingh, J. de Graauw, and Z. Olujic, "A Study of Gas and Liquid Distributions in Structured Packings," *Chemical Engineering & Technology* 12, no. 1 (1989): 445–449.

4. I. Mohammed, T. Bauer, M. Schubert, and R. Lange, "Gas–Liquid Distribution in Tubular Reactors With Solid Foam Packings," *Chemical Engineering and Processing: Process Intensification* 88 (2015): 10–18.

5. J. H. Brinkmann, D. Plate, A. Merkel, V. B. Seithümmer, P. Biessey, and M. Grünewald, "Application of a Wire-Mesh Sensor for the Experimental Characterization of Liquid Distribution in Packed Columns," *Chemical Engineering Science* 242 (2021): 116721.

6. M. Lämmermann, W. Schwieger, and H. Freund, "Experimental Investigation of Gas-Liquid Distribution in Periodic Open Cellular Structures as Potential Catalyst Supports," *Catalysis Today* 273 (2016): 161–171.

7. A. Suneja and S. Roy, "Liquid Flow Distribution in Trickle Bed Reactors Containing Trilobed Extrusions Packed Using Different Techniques," *Results in Engineering* 17 (2023): 100704.

8. U. Hampel, M. Schubert, A. Döß, et al., "Recent Advances in Experimental Techniques for Flow and Mass Transfer Analyses in Thermal Separation Systems," *Chemie Ingenieur Technik* 92, no. 7 (2020): 926–948.

9. T. Eda, A. Sapkota, J. Haruta, M. Nishio, and M. Takei, "Experimental Study on Liquid Spread and Maldistribution in the Trickle Bed Reactor Using Electrical Resistance Tomography," *Journal of Power and Energy Systems* 7, no. 2 (2013): 94–105.

10. D. Toye, M. Crine, and P. Marchot, "Imaging of Liquid Distribution in Reactive Distillation Packings With a New High-Energy X-Ray Tomograph," *Measurement Science and Technology* 16, no. 11 (2005): 2213–2220.

11. A. Fathiganjehlou, K. A. Buist, E. A. J. F. Peters, L. A. H. J. de Graaf, and J. A. M. Kuipers, "Magnetic Resonance Imaging of Trickle Flow," *AIChE Journal* 70, no. 5 (2024): e18352, https://doi.org/10.1002/aic.18352.

12. A. Sederman, P. Alexander, and L. Gladden, "Structure of Packed Beds Probed by Magnetic Resonance Imaging," *Powder Technology* 117, no. 3 (2001): 255–269.

13. A. J. Sederman and L. F. Gladden, "Magnetic Resonance Imaging as a Quantitative Probe of Gas–Liquid Distribution and Wetting Efficiency in Trickle-Bed Reactors," *Chemical Engineering Science* 56, no. 8 (2001): 2615–2628.

14. M. H. Sankey, D. J. Holland, A. J. Sederman, and L. F. Gladden, "Magnetic Resonance Velocity Imaging of Liquid and Gas Two-Phase Flow in Packed Beds," *Journal of Magnetic Resonance (San Diego, Calif: 1997)* 196, no. 2 (2009): 142–148.

15. J. F. Billingham and M. J. Lockett, "A Simple Method to Assess the Sensitivity of Packed Distillation Columns to Maldistribution," *Chemical Engineering Research and Design* 80, no. 4 (2002): 373–382.

16. Z. Olujic, R. Van Baak, and J. Haaring, "Liquid Distribution Behaviour of Conventional and High Capacity Structured Packings," in *Institution of Chemical Engineers Symposium Series* 152 (Institution of Chemical Engineers; 1999, 2006), 252.

17. H. Schoenmakers and L. Spiegel, "Laboratory Distillation and Scale-Up," in *Distillation* (Elsevier, 2014), 319–339.

18. D. P. Edwards, K. R. Krishnamurthy, and R. W. Potthoff, "Development of an Improved Method to Quantify Maldistribution and Its Effect on Structured Packing Column Performance," *Chemical Engineering Research and Design* 77, no. 7 (1999): 656–662.

19. F. Hanusch, M. Künzler, M. Renner, S. Rehfeldt, and H. Klein, "Liquid Distributor Design for Random Packed Columns," *Chemical Engineering Research and Design* 147 (2019): 689–698.

20. F. Moore and F. Rukovena, "Liquid and Gas Distribution In Commercial Packed Towers," *Chemical Plants and Processing* 8 (1987): 11–15.

21. L. Spiegel, "A New Method to Assess Liquid Distributor Quality," *Chemical Engineering and Processing: Process Intensification* 45, no. 11 (2006): 1011–1017.

22. R. N. Maiti and K. D. P. Nigam, "Gas−Liquid Distributors for Trickle-bed Reactors: A Review," *Industrial & Engineering Chemistry Research* 46, no. 19 (2007): 6164–6182.

23. L. Spiegel and M. Duss, "Structured Packings," in *Distillation* (Elsevier, 2014), 145–181.

24. C. Tony, "Pour Point Density Estimations for Packed Columns With Structured Packing," *Chemical Engineering Transactions* 69 (2018): 709–714.

25. Ž. Olujić and H. Jansen, "Large-Diameter Experimental Evidence on liquid (Mal)Distribution Properties of Structured Packings," *Chemical Engineering Research and Design* 99 (2015): 2–13.

26. R. Goedecke, ed., *Fluidverfahrenstechnik: Grundlagen, Methodik, Technik, Praxis* (Wiley, 2006), https://onlinelibrary.wiley.com/doi/book/10.1002/9783527623631.

27. W. Hofen, M. Körfer, and K. Zetzmann, "Scale–up–probleme bei der experimentellen verfahrensentwicklung," *Chemie Ingenieur Technik* 62, no. 10 (1990): 805–812.

28. M. A. Ashour, J. Neukäufer, N. Sarajlic, et al., "Flexible 3D–Printed Test Rig for Liquid Distribution Characterization of Laboratory-Scale Packings," *Chemie Ingenieur Technik* 94, no. 7 (2022): 1010–1016.

29. S. Da Cunha, B. Dejean, B. Mizzi, N. Shcherbakova, D. Rouzineau, M. Meyer, and V. Gerbaud, "Design, Conception, and Assessment of an Innovative Liquid Distributor for Separation Column," *Chemical Engineering Research and Design* 196 (2023): 377–389.

30. B. Sun, T. Bhatelia, R. P. Utikar, G. M. Evans, and V. K. Pareek, "Hydrodynamics of a Novel 3D Printed Structured Packing–Spiropak," *Chemical Engineering and Processing: Process Intensification* 167 (2021): 108533.

31. N. E. Daidzic, E. Schmidt, M. M. Hasan, and S. Altobelli, "Gas–Liquid Phase Distribution and Void Fraction Measurements Using MRI," *Nuclear Engineering and Design* 235, no. 10-12 (2005): 1163–1178.

32. B. E. Rapp, "Plateau-Rayleigh Instability," in *Microfluidics: Modelling, Mechanics and Mathematics* (Elsevier, 2017), 467–477.

33. P. K. Kundu, I. M. Cohen, and D. R. Dowling, "Instability," in *Fluid Mechanics* (Elsevier, 2016), 533–602.

34. Ž. Olujić, "Types of Distillation Column Internals," in *Distillation* (Elsevier, 2014), 1–34.

35. R. K. Singh, J. Bao, C. Wang, Y. Fu, and Z. Xu, "Hydrodynamics of countercurrent Flows in a Structured Packed Column: Effects of Initial Wetting and Dynamic Contact Angle," *Chemical Engineering Journal* 398 (2020): 125548.